Interpretative Framework for CPT p-y Module Tests in Drained

Sands: A Practical Model for End Effect Elimination Considering

Sand Relative Density and Surcharge Pressure

Kai Wen, PhD.; Research Fellow in Offshore Geotechnical Engineering; k.wen@soton.ac.uk

Department of Civil, Maritime and Environmental Engineering, University of Southampton,

Southampton SO16 7QF, UK

David J. White, Ph.D.; Professor of Infrastructure Geotechnics; david.white@soton.ac.uk

Department of Civil, Maritime and Environmental Engineering, University of Southampton,

Southampton SO16 7QF, UK

Benjamin Cerfontaine, Ph.D.; Lecture in Geotechnical Engineering; b.cerfontaine@soton.ac.uk

Department of Civil, Maritime and Environmental Engineering, University of Southampton,

Southampton SO16 7QF, UK

Susan Gourvenec, Ph.D.; Professor of Offshore Geotechnical Engineering;

susan.gourvenec@southampton.ac.uk

Department of Civil, Maritime and Environmental Engineering, University of Southampton,

Southampton SO16 7QF, UK

Andrea Diambra, Ph.D.; Professor of Geotechnical Engineering; Andrea.Diambra@bristol.ac.uk

Department of Civil Engineering, University of Bristol, BS8 1TR Bristol, UK

Article type: General paper

Main text length (from Introduction to Conclusions, 6230 words)

Number of Figures: 17

1

1 ABSTRACT

- 2 Accelerating the current timeline of offshore wind projects is imperative to achieve global 3 decarbonisation plans. In response, a novel in-situ site characterisation tool ROBOCONE is being 4 developed to make the geotechnical design of offshore pile foundations more efficient by directly 5 providing lateral p-y response data, reducing the need for offshore sampling and onshore laboratory 6 testing. This device expands the kinematic range of standard cone penetrometer testing by integrating 7 a robotic cylindrical section capable of horizontal translation, referred to as a p-y module. However, 8 due to the finite length of p-y module, it is necessary to quantify 'end effects' to accurately derive p-y 9 curves from the direct measurements of the p-y module. This paper presents detailed three-dimensional 10 finite element analyses of the p-y module in sands, utilizing a bounding surface elastoplastic model that 11 accounts for variations in stress-strain behaviour due to density and stress level. The resulting end effect model is underpinned by a two-stage optimisation process that considers key factors such as overburden 12 pressure and relative density. The model's predictive accuracy is proven through additional finite 13 14 element analyses different to the calibration cases. The research outcomes offer a robust interpretative 15 framework to accurately determine p-y curves for the design of laterally loaded offshore piles, using 16 the ROBOCONE p-y module.
- 17 **Keywords**: numerical modelling; offshore site investigation; ROBOCONE p-y module; sands; end
- 18 effect; p-y curves

INTRODUCTION

19

20

21

22

23

24

25

26

27

28

29

30

31

32

33

34

35

36

37

38

39

40

41

42

43

44

The UK's long-term vision to achieve net-zero emissions necessitates up to 125GW offshore wind capacity to be installed by 2050 (CCC 2020), which is around seven times the current capacity of 15 GW at the end of 2023. To support this rapid growth, there is a pressing need to compress the typical timeline of offshore wind farm developments, which is currently around 15 years from site leasing to operation in the UK (Greaves et al 2024). From the perspective of geotechnical practice, one of the crucial targets is enhancing the efficiency of the processes for site characterisation and design for offshore foundations. Driven piles are commonly utilised as offshore foundations for bottom-fixed wind turbines and can also serve as anchors for offshore floating platforms. In current design practice, the serviceability response to lateral loads is typically predicted using the 'p-y' spring approach. This approach involves dividing the pile into a series of segments and idealising the continuum soil domain into a series of independent nonlinear soil springs that represents the mobilisation of local lateral resistances, p, with local pile displacement, y (Matlock 1970; API 2014; DNV GL 2016; Burd et al. 2020; Jeanjean 2009). When establishing p-y curves at a specific site, it is common to correlate the cone penetration test (CPT) measurements to the stiffness and strength parameters needed for the p-y curves in advance of detailed soil laboratory testing (Suryasentana and Lehane 2014; Guo and Lehane 2016; Lehane 2019). However, it is recognised that the soil failure mechanisms and stress paths that govern CPT parameters do not match those controlling laterally pile-soil response parameters (Diambra et al. 2022). A collaborative research project 'ROBOCONE' has developed a prototype of new site investigation tool by adding a cylindrical 'p-y' module section into the standard CPT equipment, as shown in Figure 1 (White 2022; Diambra et al. 2022; Creasey et al. 2022). This device, capable of horizontal translation, expands the kinematic range of CPT testing and allows to probe the soil response to more representative stress histories, drawing on advancements in robotic control and actuation. This innovative equipment can accelerate the pile design process in two aspects: (i) by providing in-situ characterisation of soil properties, eliminating the challenges of sample disturbance and recapturing in situ stress states during laboratory testing and (ii) direct extracting the p-y curves to support the design of laterally loaded piles, relying on the similarity of the soil deformation pattern near the p-y module and a pile elements (see Fig 1). Wen et al. (2024) adopted approach (i) via an interpretive framework to convert measured ROBOCONE data into soil properties such as undrained shear strength and elastic stiffness.

This paper will tackle the approach (ii) and address the challenge of additional soil reaction due to the finite length of the p-y module and the resulting displacement discontinuity between the stationary penetrometer shaft and the moveable p-y module – referred hereafter as the end effect. It is necessary to eliminate such end effect from the p-y module measurements in order to obtain practical p-y curves for the design of laterally loaded piles.

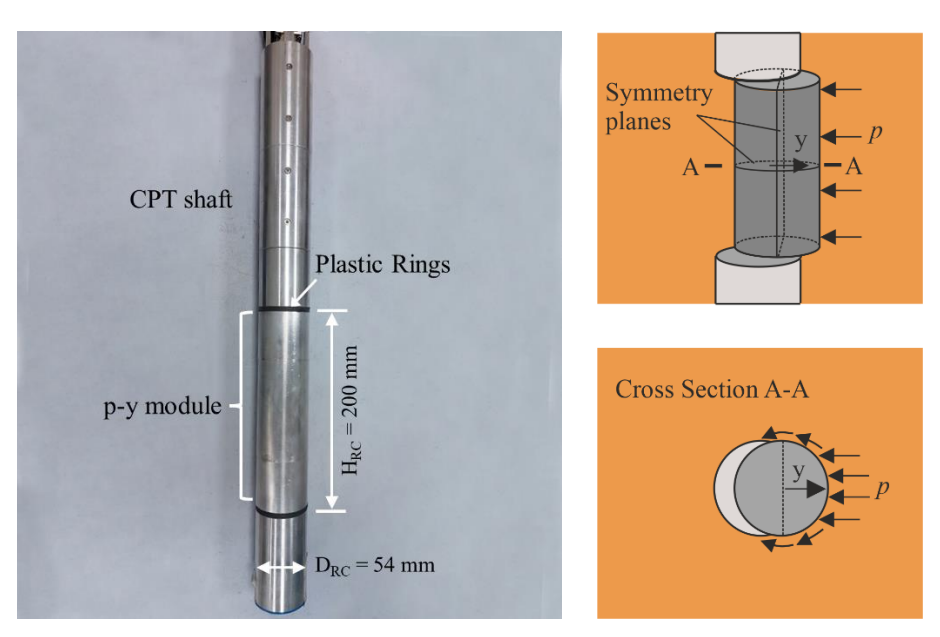


Figure 1 Schematic illustration of ROBOCONE p-y module (adapted from Diambra et al. 2022)

Finite element (FE) modelling is widely used to develop interpretative frameworks for novel in-situ characterisation tools, including T-bar penetrometers (Randolph and Andersen 2006, White et al. 2010, Zhu et al. 2020, Wang et al. 2022), ball penetrometers (Zhou et al. 2013; Mahmoodzadeh et al. 2015) and shallow penetrometers – such as the hemiball and toroidal (Yan et al. 2011, Stanier & White 2015). The ROBOCONE p-y module is a new concept, and this paper contributes the first analyses of such a device in drained cohesionless material.

The objective of this paper is to develop an interpretative framework of accurately predicting, and eliminating, the end resistance contribution to the measured resistance on a p-y module in drained sands,

thus providing the resistance equivalent to the p-y spring. Three-dimensional FE modelling of a p-y module subject to monotonic lateral movement is carried out, including a comprehensive parametric study with a wide range of geometries and soil conditions, including variations in density, and overburden or surcharge pressure. The resulting end effect model allows the deduction of end resistance from p-y module measurements thus providing rational p-y curves for offshore pile design.

FINITE ELEMENT MODEL

64

65

66

67

68

69

70

71

72

73

74

75

76

77

78

79

80

81

82

83

84

85

86

87

88

89

effects.

Model geometry and boundary conditions

The three-dimensional finite element (FE) analyses in this study were carried out in the PLAXIS 3D V23 programme (PLAXIS 2023). Figure 2 illustrates the geometry of the ROBOCONE system, including the CPT shaft and moveable p-y module. These structures are wished-in-place, neglecting the impact of the installation process. In the prototype ROBOCONE, a stack of moveable discs is installed at each end of the p-y module to prevent water leakage and soil particles from entering the CPT rod (Creasey et al. 2023). However, these discs were omitted in this study in order to improve the numerical stability of FE analyses. Analyses indicate this simplification has a negligible impact on the loaddisplacement response. Using the double symmetry of the simulated problem (see Figure 1), only a quadrant of p-y module was simulated to reduce the computational cost while ensuring accuracy. Although the actual p-y module prototype is a hollow cylindrical shaft with a complex actuation system and sensors inside (Creasey et al. 2023), it was modelled as a solid rigid body for simplicity as the mechanical operation of the device is not relevant for the analysis of the soil response. The prototype p-y module, featured an external diameter (D_{RC}) of 54 mm and a height (H_{RC}) of 100 mm, is embedded within a half-cylindrical soil domain measuring 2600 mm in diameter and 1100 mm in thickness. These soil dimensions were determined after sensitivity studies of possible domain boundary effect on p-y module response. It is important to note that any variations in the module dimensions (H_{RC}, D_{RC}) , as discussed subsequently, require corresponding alterations in the soil domain dimensions to ensure the elimination of boundary

The soil was discretised using second-order tetrahedral elements, each with 10-nodes and four Gaussian integration points. A relatively finer discretisation was applied near the p-y module to avoid stress concentrations and reduce the influence of element size. Two planes of symmetry at Y = 0 and Z = 0 were normally fixed to prevent orthogonal movements, while vertical displacements were permitted along the curved side of the soil domain and at the top surface.



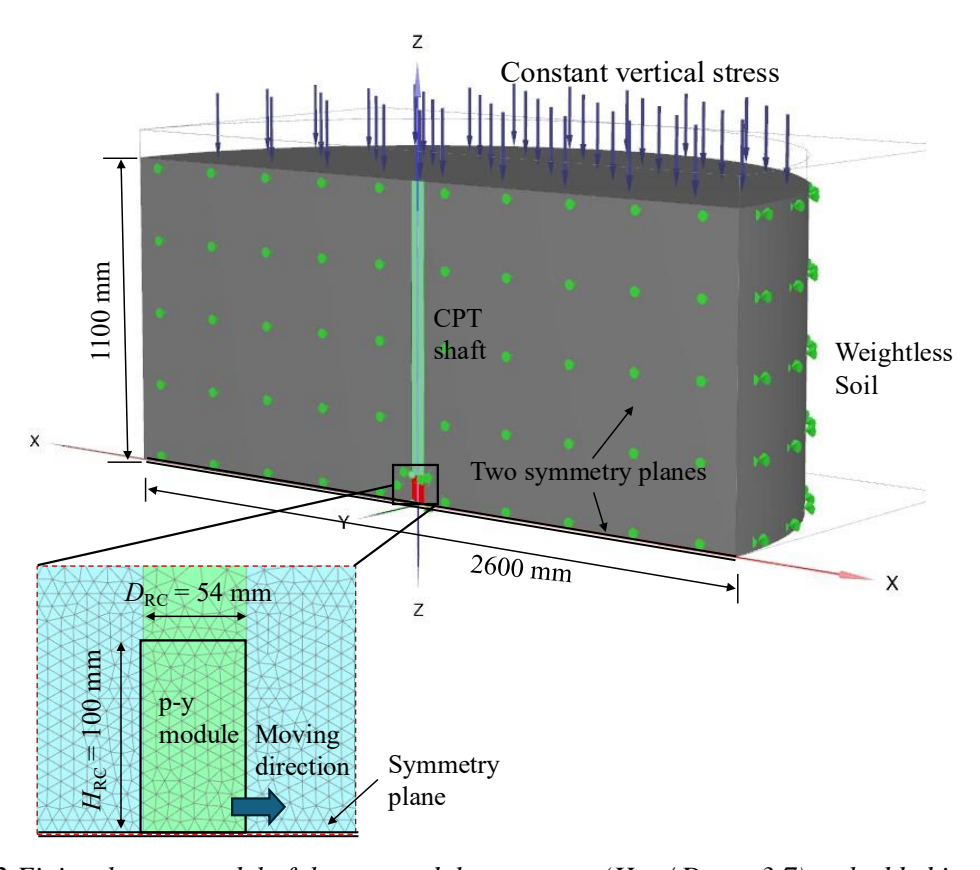


Figure 2 Finite element model of the p-y module prototype ($H_{RC}/D_{RC}=3.7$) embedded in soil assembly with mesh, loading and boundary conditions

The ROBOCONE system was modelled as a rigid body with all degrees of freedom fixed, except for a lateral translation in the X-direction which was prescribed. The stress-strain response of the soil domain was represented by a bounding surface plasticity model in fully drained conditions, as detailed later. Zero-thickness interface elements were introduced around the p-y module to reflect the soil-structure interaction, which allows separation between the structure and soil to occur (PLAXIS 2023). The interface was modelled using an elasto-plastic Mohr-Coulomb model, with the elastic parameters of shear stiffness K_s = 4.5E6 kN/m³ and normal stiffness K_n = 5.1E7 kN/m³. These stiffness parameters

were determined after a sensitivity study that ensured they have negligible influence on the p-y module response. The plastic parameters included a nominal cohesion of $c'_i = 3$ kPa (ensuring numerical stability) and an effective angle of shearing resistance $\varphi'_i = 29.0^\circ$.

Constitutive model

The SANISAND-MS constitutive model (Liu et al. 2019) was selected to represent the drained sand stress strain behaviour. It is a bounding surface elastoplastic model, based on a critical state framework. The model is an evolution of the SANISAND04 model (Dafalias and Manzari 2004) to accurately capture the response under long-term cyclic loading. It has been preferred over the parent model due to its enhanced versatility for future studies of the ROBOCONE p-y module under complex and cyclic loading paths. Nevertheless, the response under monotonic loading is identical to that of the parent SANISAND04 model. The monotonic plastic response is governed by four distinct conical surfaces (Figure 3). They are (1) the yielding surface, controlling the boundary of the elastic region; (2) the dilatancy surface, defining the transition from plastic contraction to dilation; (3) the critical state surface, defining the stress conditions at failure and (4) the bounding surface, defining the peak strength and the plastic strain rate. This SANISAND models' family captures the effect of void ratio and mean effective stress, p', on strength and stiffness with a single set of parameters.

The model adopts a hypoelasticity law for its elastic behaviour, where the elastic shear and bulk modules $(G_0 \text{ and } K)$ are functions of mean effective stress p' and current void ratio e (Richart et al., 1970; Li and Dafalias, 2002).

$$G_0 = G_0' p_{\text{atm}} \left[\frac{(2.97 - e)^2}{(1 + e)} \right] \sqrt{\frac{p'}{p_{\text{atm}}}}$$
 (1)

$$K = \frac{2}{3} \left(\frac{1+\nu}{1-2\nu} \right) G_0 \tag{2}$$

where G'_0 is a dimensionless input parameter; ν is a constant Poisson's ratio.

There are 11 primary model parameters employed to characterise the plasticity component of the SANISAND-MS model under monotonic loading and three additional parameters governing the

response under cyclic loading. These parameters and the main modelling features are briefly introduced below:

- (a) The yield surface is a narrow cone in stress space, of a constant opening defined by the model parameter *m*. When the soil starts yielding, the inclination of the yield locus can change to maintain the soil stress state on its boundary. Consequently, the elastic region moves together with the changes in the mobilised stress ratio, as the model utilises only kinematic hardening.
- (b) The opening of the critical state surface is defined by the stress ratios q/p corresponding to the strengths in triaxial compression and tension at critical state, denoted as M_e and M_c respectively. The model parameter c defines the ratio of M_e/M_c .
- (c) The opening of the bounding surface (M^b) influences the peak strength of sand, and it is related to opening of the critical state surface through the state parameter ψ , defined as the difference between the current void ratio, e, and that at the critical state line (e_{cs}) under the same p', as given by:

$$\psi = e - e_{\rm CS} = e - \left[e_0 - \lambda \left(\frac{p'}{p_{\rm atm}} \right)^{\xi} \right]$$
 (3)

where the model parameter e_0 represents the void ratio at the critical state for p'=0; ξ and λ are input parameters that control the shape of the critical state line in the e-ln p' plane (Li & Wang 1998; Dafalias & Manzari 2004). Hence, the opening angle of the bounding surface in triaxial compression is: $M^b = M_c \cdot \exp\left(\langle -\psi \rangle n^b\right)$, where n^b is an input parameter. Note that $\langle -\psi \rangle = -\psi$ if $\psi < 0$ and $\langle -\psi \rangle = 0$ if $\psi > 0$. For very dense sands ψ is generally a large negative number, which allows a very high stress ratio to characterise the bounding surface, thus providing a high peak strength.

(d) The dilatancy (i.e. the ratio between plastic volumetric strain and plastic deviatoric strain) depends on the deviatoric distance between the current stress state and the dilatancy surface and a model parameter A_0 . This means the soil contracts when inside the dilatancy surface and dilates outside. A dilatancy surface with inclination M^d in the p'-q plane depends also on ψ and

an input parameter n^d , as given by $M^d = M_c \cdot \exp{(n^d \psi)}$ in compression. For dense sands, a large negative ψ yields a lower stress ratio, implying the onset of plastic dilation occurs early during shearing.

- (e) The plastic modulus depends on the deviatoric distance from the current stress state to the bounding surface, thus dependent on the current e and p, and scaled by the model parameters h_0 and c_h .
- (f) There are three input parameters μ_0 , ζ , β related to memory surfaces and the ratcheting characteristics of sands, but they should have no influence on the mechanical response in drained monotonic loading conditions.

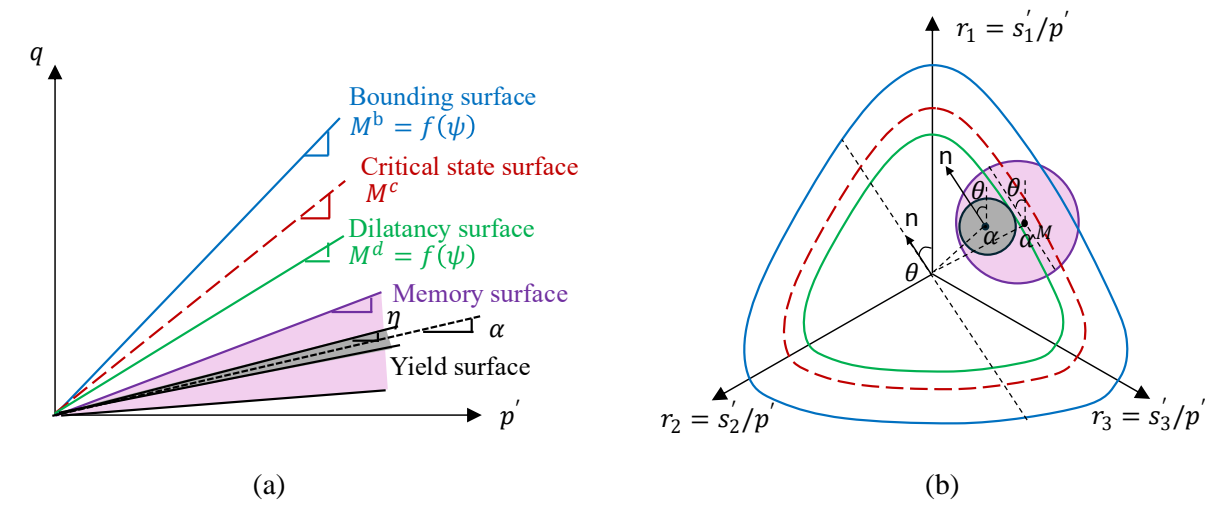


Figure 3 Schematic illustration of SANISAND-MS model surfaces (a) in p'-q space; (b) in the deviatoric stress ratio plane (modified after PLAXIS (2023))

Calibration of parameters

The value of the model parameters previously calibrated by Pisanò et al. (2024) for the simulation of monopiles in Dunkirk sand were used in this study (see Table 1). Among those, the three parameters related to the memory surface are not considered to affect the monotonic loading behaviour of ROBOCONE module. The initial void ratio (e_0) is specified as 0.6 (corresponding to $D_R = 83\%$) as a base case, which is later varied to investigate its effect of sand density on the p-y module response. The maximum and minimum void ratios were defined as the limits to the evolution of void ratio (following Kuwano 1999) to prevent unrealistic soil states.

Table 1 SANISAND-MS model parameters calibrated for Dunkirk sands (Pisanò et al. 2024) as used in this study

Components	Parameters
Elasticity	$G_0 = 451$; $v = 0.17$
Critical state line	$M_c = 1.28$; $c = 0.72$; $\lambda_c = 0.135$; $e_0 = 0.91$; $\xi = 0.18$
Yield surface	m = 0.065
Hardening modulus	$h_0 = 3.5$; $c_h = 1.0$; $n_b = 1.9$
Dilatancy	$A_0 = 1.3$; $n_d = 0.75$
Memory surface	$\mu_0 = 260; \zeta = 1E-4; \beta = 1.0$
Initial void ratio	$e_0 = 0.60$
Min and Max void ratios	$e_{min} = 0.54$; $e_{max} = 0.91$
Maximum bounding stress ratio	$M_{\text{max}}^{\text{b}} = 1.63$

Figure 4 describes the performance of the SANISAND-MS model with the set of parameters from Table 1 against measured drained triaxial tests on Dunkirk sand at relative density $D_R = 73\%$. The results demonstrate reasonable agreement between the simulations and laboratory results, underscoring the effectiveness of the constitutive model across a range of initial confining stresses.

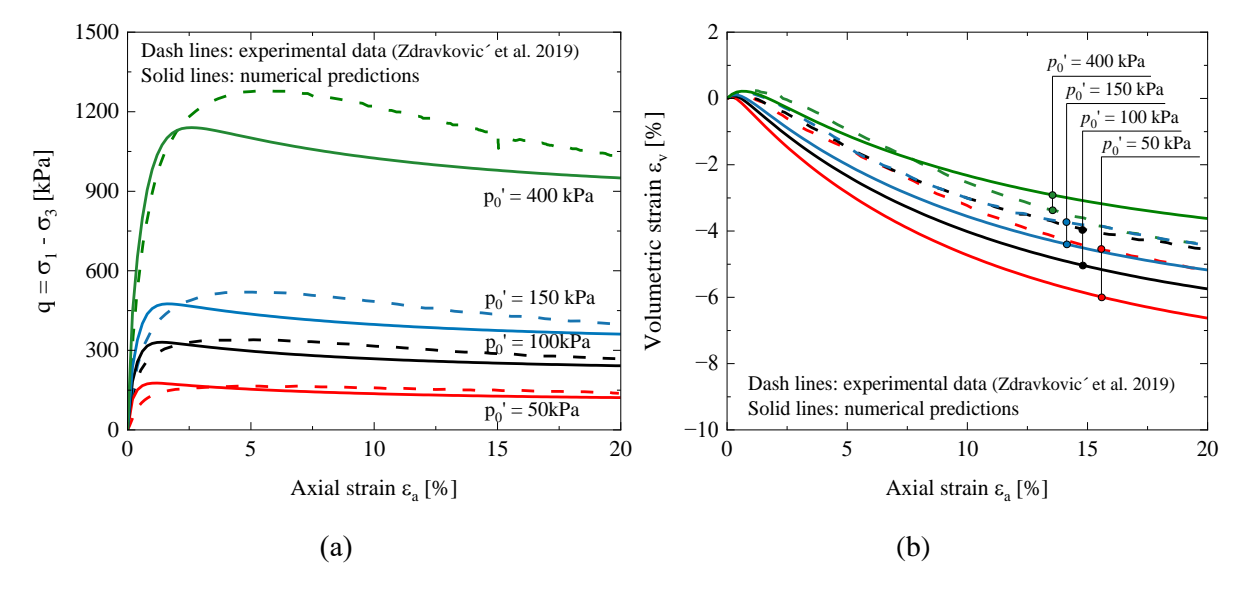


Figure 4 Performance of SANISAND-MS model on predicting the drained triaxial compression behaviour of Dunkirk sand (adapted from Pisanò et al. 2024)

Description of FE simulations

For modelling the p-y module, the initial simulation phase created an isotropic stress state in the soil domain by applying a uniform vertical surcharge pressure on the top boundary surface of the soil domain (see Figure 2) and specifying a coefficient of earth pressure at rest (K_0 = 1) to generate horizontal stress. The soil was defined as weightless so that the variations of surcharge pressure (σ'_v) on the domain

- represented different overburden stresses at the operating depth of the p-y module. In the second simulation phase, lateral displacement of the p-y module was prescribed in the X direction.
- The main objective of the analyses is to quantify the end effect due to the finite length of the ROBOCONE p-y module. To achieve this, two different types of simulation were undertaken, as illustrated in Figure 4.

- Case A, consistent with the field conditions: a lateral monotonic displacement along the X-direction is prescribed to the reference point of the rigid p-y module, while the CPT shaft is fixed in all degrees of freedom.
- Case B: a lateral monotonic displacement along the X-direction is prescribed to the reference points of both the rigid p-y module and the CPT shaft, ensuring zero relative displacement between the moveable p-y module and the CPT shaft, causing no end effect to occur.

In both cases, the resultant reaction force acting on the ROBOCONE p-y module were directly extracted at the reference points of horizontal translation, which corresponds to the total force F_{tot} in the Case A and to the net force F_{net} in the Case B. The reaction forces were then divided by the ROBOCONE projected area ($D_{\text{RC}}H_{\text{RC}}$) to obtain the p-values, as illustrated in Figure 5, denoted as p_{tot} and p_{net} in Case A and Case B respectively. In comparison to the Case A, the p_{net} -y curves from Case B were considered to contain zero end effects, given there is no relative motion between ROBOCONE p-y module and CPT shaft. As such, the soil layers above and below the p-y module exhibits negligible interaction with the soil zone at the elevation of the module because their horizontal movements are equal. This aligns well with the original definition of the p-y approach, in which the soil domain is idealised into a series of independent Winkler-type springs acting on the lateral piles (Reese et al. 1974). Hence, p_{net} -y curves in the Case B are what the users of ROBOCONE need in order to facilitate the design of offshore laterally loaded piles.

The total ROBOCONE resistances in Case A are therefore the superposition of two components, i.e. the Case B net ROBOCONE resistance plus the additive resistances due to end effect $p_{\rm EE}$, so that:

$$p_{EE} = \frac{F_{tot} - F_{net}}{D_{RC}H_{RC}} = p_{tot} - p_{net}$$

$$\tag{4}$$

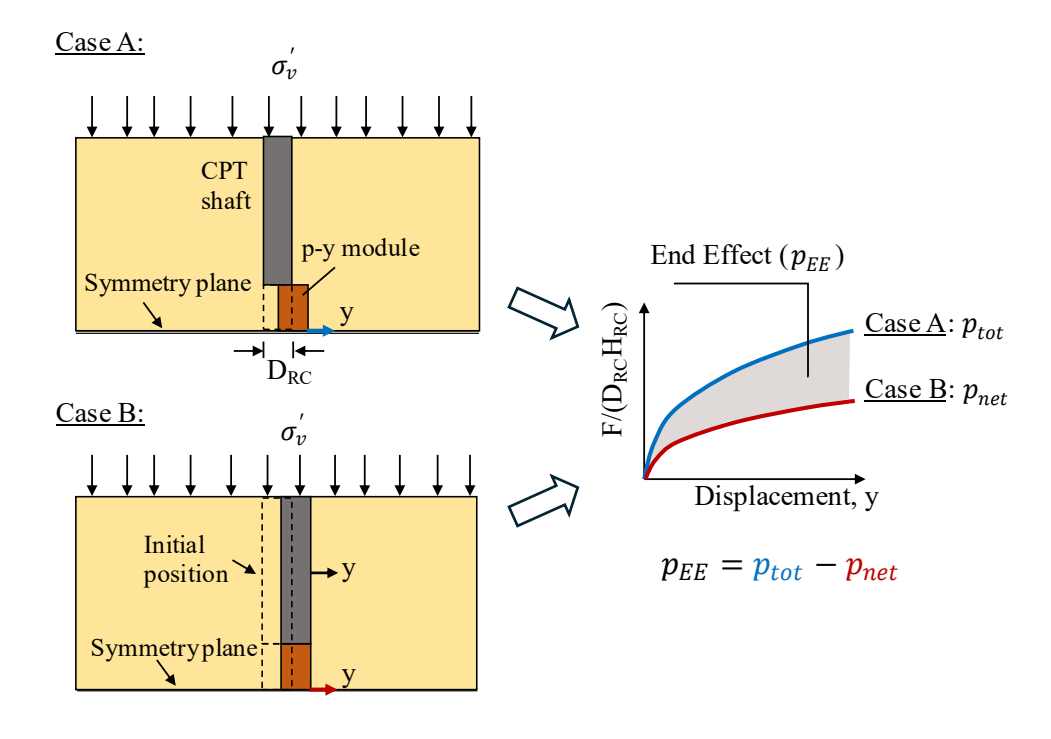


Figure 5 Determination of end effects from comparison of FE analysis cases

RESULTS & DISCUSSION

The mechanisms related to the end effect of the ROBOCONE p-y modules are first identified, and the main influencing parameters discussed, including aspect ratio (H_{RC}/D_{RC}), sand relative density (D_R) and surcharge pressure (σ'_V). An interpretative framework is then developed based on a parametric study for a p-y module with aspect ratio $H_{RC}/D_{RC}=3.7$, which corresponds to the prototype ROBOCONE (Creasey et al. 2022).

Key features of ROBOCONE p-y module response

Aspect ratio is an important geometric feature of the ROBOCONE. A high aspect ratio reduces the relative contribution of the end effect to the measured total force, which is beneficial. However, the force required to move the p-y module increases with its length and is limited by the capacity of the actuation system that has to be miniaturised in order to fit in the standard CPT rod.

Figure 6 illustrates the numerical total resistances (p_{tot} , Case A) and net resistances (p_{net} , Case B) of ROBOCONE and the calculated end effect (p_{EE} , Eq. (4)), for a selected surcharge pressure $\sigma'_{v} = 200$ kPa and relative density $D_R = 83\%$. The p-y module reaction forces are divided by the product of the height and diameter of the ROBOCONE module, $H_{RC}D_{RC}$, and the lateral displacement is normalised by D_{RC} . Three different aspect ratios, $H_{RC}/D_{RC} = 3.7$ (prototype), 8.0 and 16.0, were tested.

Figure 6 shows the total resistance (p_{tot}) decreases with the aspect ratio. However, the p_{net} -y curves are almost identical, regardless of the aspect ratio of the ROBOCONE. The relative contribution of the end effect to the ROBOCONE p_{tot} appear to vary as a function of the aspect ratio. For instance, the ratio of p_{EE}/p_{tot} at $y/D_{RC} = 35\%$ reduces from 39% for the shortest p-y module ($H_{RC}/D_{RC} = 3.7$) to 20% for the longest p-y module ($H_{RC}/D_{RC} = 16.0$). Moreover, the relative importance of the end effects in the measured ROBOCONE resistances (p_{tot}) tend to vary as a function of the normalised y/D_{RC} . At small displacement, the net resistance component (p_{net}) dictates the magnitudes of total resistances, while the end effects become more prominent in a later stage of the p-y module displacement. Therefore, any end effect correction of the measured ROBOCONE data should include this dependency.

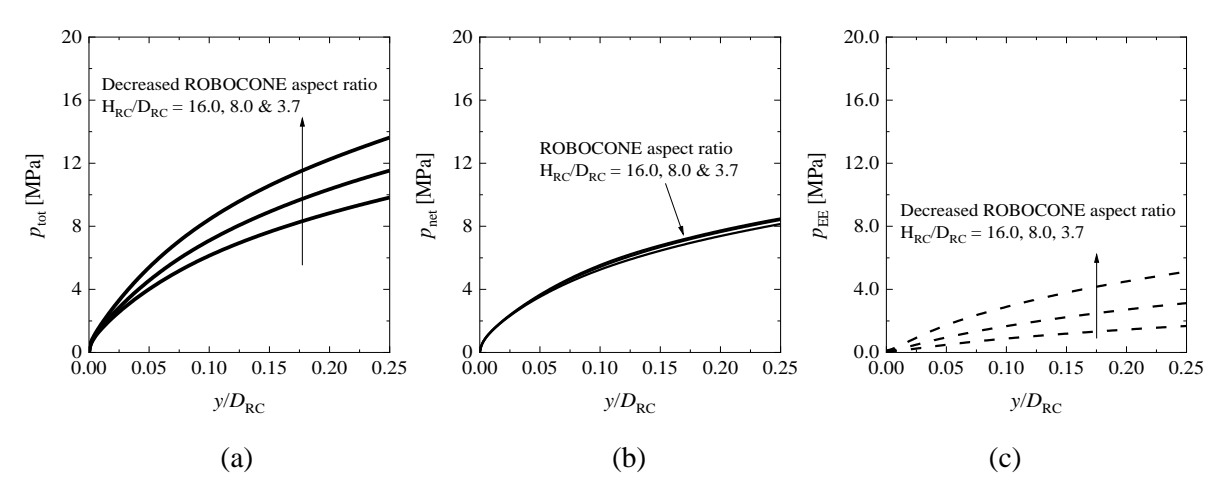


Figure 6 Monotonic loading response of p-y module with various aspect ratios ($\sigma'_v = 200 \text{ kPa}$; $D_R = 83\%$): (a) p_{tot} -y curves; (b) p_{net} -y curves; (c) p_{EE} -y curves

The stress p_{EE} above is expressed as the calculated end effect force F_{EE} divided by the projected area of ROBOCONE (H_{RC}D_{RC}) in the translating direction. As with Wen et al. (2024), another more meaningful and straightforward way is to present end resistances in the form of $\tilde{p}_{EE} = F_{EE}/D_{RC}^2$, which

excludes the impact of the ROBOCONE length so is a better quantity to describe the end effect. By doing so, the Figure 6(c) can be converted to investigate relationship between \tilde{p}_{EE} and aspect ratio. As shown in Figure 7, the evolution of \tilde{p}_{EE} tend to converge at greater H_{RC}/D_{RC} , which implies some degree of interaction between the two ends for lower aspect ratios.

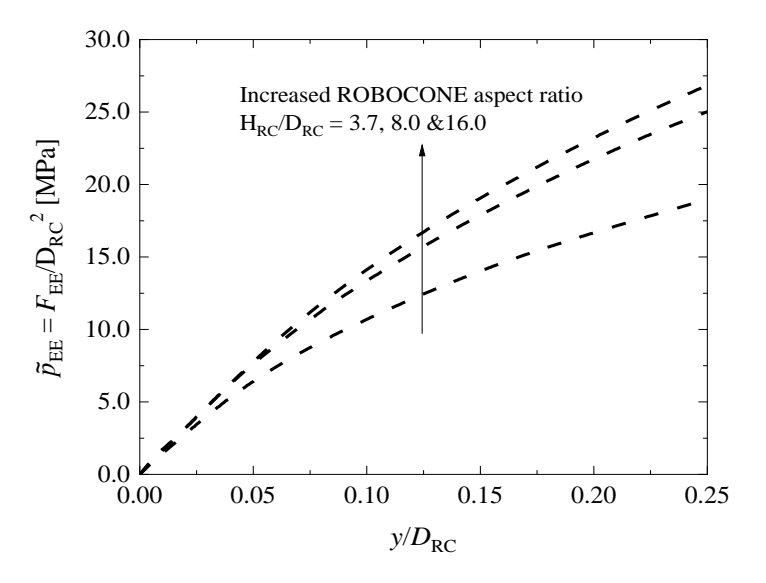


Figure 7 Variation of end resistance with increasing lateral displacement and ROBOCONE p-y module aspect ratios ($\sigma'_v = 200 \text{ kPa}$)

Figure 8 demonstrates the influence of surcharge pressure ($\sigma'_{\rm v}$) on the p-y module response components, of total, net and end resistances respectively. Higher stress levels lead to increased resistance and initial stiffness, as captured in the SANISAND-MS model by the frictional nature of soil resistance and the stress dependent soil stiffness defined in Eq. (1). The contribution of the end effect ($p_{\rm EE}$) to the total ROBOCONE resistance ($p_{\rm tot}$) decreases with an increasing surcharge stress $\sigma'_{\rm v}$. For instance, at a normalised displacement $y/D_{\rm RC}=30\%$, the end effect accounts for approximately 50% of the total resistance at low surcharge stress $\sigma'_{\rm v}=10$ kPa, reducing to around 40% at $\sigma'_{\rm v}=200$ kPa.

While most p-y models for pile design include a plateau in p values in drained sands (e.g., API 2014; Burd et al. 2020), the only simulation that reached a stable upper limit of p_{RC} was for a surcharge stress $\sigma'_{V} = 10$ kPa, at a displacement of $25\%D_{RC}$, which approaches the lateral translation limit of the prototype ROBOCONE, which is $20\%\sim25\%D_{RC}$ (Creasey et al. 2022). This effect can be attributed to the progressive suppression of the soil's tendency to dilate during shearing due to the confining pressure from the surrounding mass. As the soil tends to dilate within a confined mass, the surrounding confining

stress increases, leading to a corresponding increase in the soil's shear strength. This process continues until the shear strength reaches a plateau when the soil attains its critical state conditions. This increase will be higher and take longer for deep embedment depth ($\sigma'_v = 200 \text{kPa}$) due to the higher soil stiffness and larger volume of surrounding soil mass involved. Indeed, the plateaus observed in p-y curves backfitted to full-scale pile load tests are located close to the surface (at low vertical stress), where a shallow mechanism develops. It can therefore be assumed that the variation of surcharge pressure is a simple way to represent the change in response of the p-y module at different operation depths.

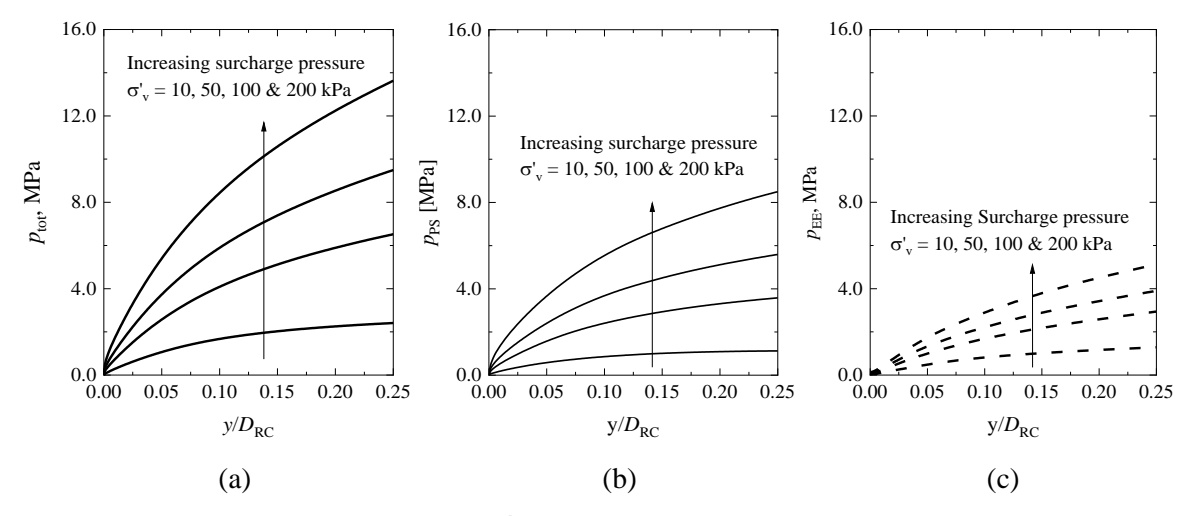


Figure 8 Impact of surcharge pressure σ'_v on the p-y module response (H_{RC}/D_{RC} = 3.7; D_R = 83%): (a) total resistances p_{tot} ; (b) net resistances p_{net} ; (c) end effect resistances p_{EE}

End effect mechanism

The vertical soil displacement during translation of the p-y module is an indicative way to show the influence zone and three-dimensional nature of the end effects. Figure 9 shows the profile of soil displacement in the symmetry plane of the p-y module at a displacement of 20% $D_{\rm RC}$, with $H_{\rm RC}/D_{\rm RC}$ = 3.7, 8.0 and 16.0. The zones of vertical displacement retain a similar shape independent of the aspect ratios, while their dimensions show slight variations. Those vertical displacement zones overlap with the volume of soil directly in front of the p-y module and indicate that some degree of interaction exists between the two p-y components ($p_{\rm EE}$ and $p_{\rm PS}$). The vertical displacement of the soil closer to the symmetry line is close to zero, especially at larger aspect ratios.

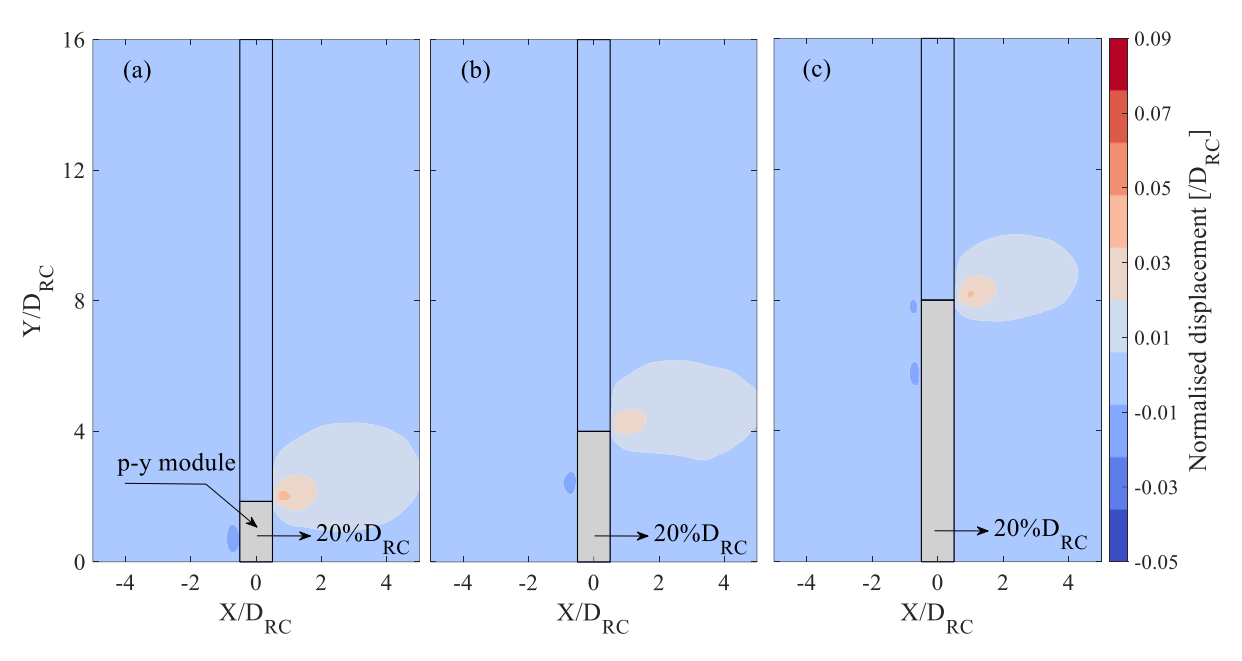


Figure 9 Fields of cumulative vertical soil displacement at $y/D_{RC}=20\%$: (a) $H_{RC}/D_{RC}=3.7$; (b) $H_{RC}/D_{RC}=8.0$; (c) $H_{RC}/D_{RC}=16.0$

Figure 10 shows the distribution of current void ratio surrounding the p-y module at the longitudinal cross section (y = 0). The void ratio is incorporated as a state variable in the SANISAND-MS model and capable of visualising the soil zones influenced by the p-y module movement. The sand domain at the front of the p-y module experiences dilation, i.e., an increase in void ratio (relative to initial e_0 = 0.60), owing to the dilation of the dense sand (initially D_R = 83%). Behind the p-y module, where the soil is experiencing unloading, an increase in void ratio can be observed for all cases.

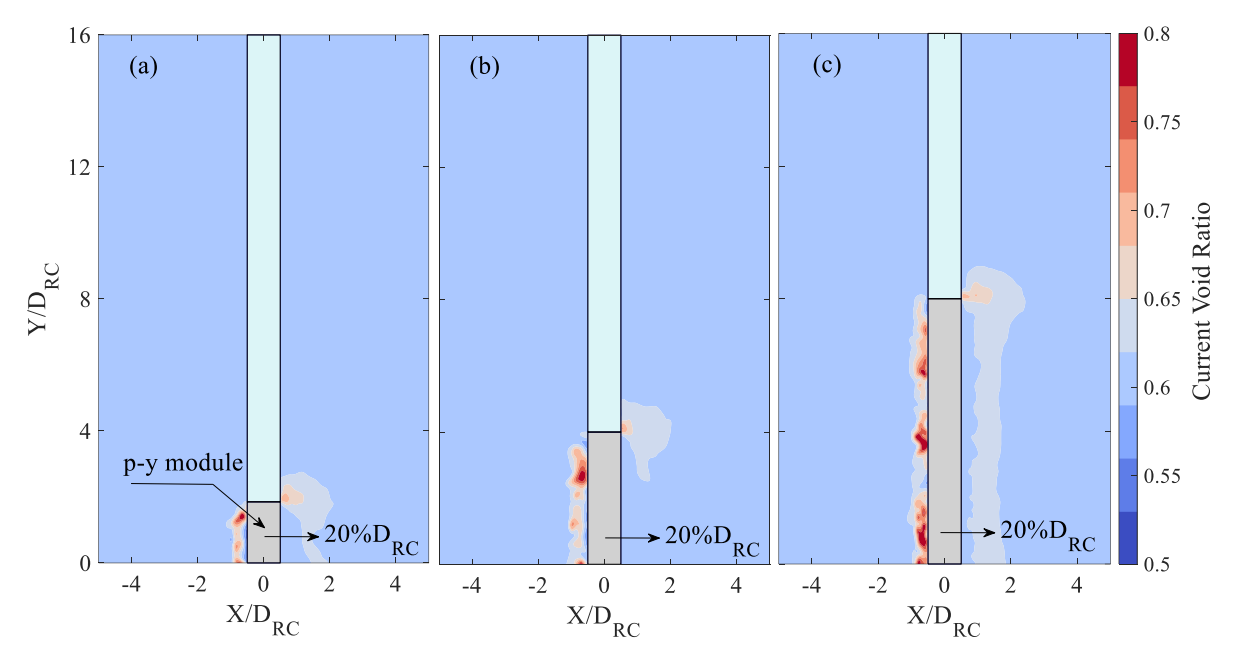


Figure 10 Fields of current void ratio at $y/D_{RC} = 20\%$: (a) $H_{RC}/D_{RC} = 3.7$; (b) $H_{RC}/D_{RC} = 8.0$; (c) $H_{RC}/D_{RC} = 16.0$

End effect model

The purpose of the ROBOCONE tool is to determine p_{net} -y curves directly in situ. This requires correction of the measured p_{tot} -y curves to remove the end effect contribution across the full range of lateral displacements. The following section details this correction framework for monotonic loading, for the aspect ratio corresponding to the dimensions of the prototype p-y module ($H_{\text{RC}}/D_{\text{RC}} = 3.7$) (Creasey et al. 2022). The calibration space, as set out in $Table\ 2$, consisting of 12 combinations of surcharge pressure (σ'_{V} , from 10 kPa to 200 kPa) and relative densities (D_{R} , from 43% to 83%). For each combination, a pair of FE analyses were undertaken (Cases A and B), to calculate the end effect contribution \tilde{p}_{EE} . All individual curves were fitted by an explicit conic function (Equations (5), (6)), which has been used to capture the p-y soil response from small to large displacements and has been widely adopted by the offshore industry (Burd et al. 2020).

$$\tilde{p}_{\text{EE}} = \tilde{p}_{u,EE} \frac{2c}{-b + \sqrt{b^2 - 4ac}} \qquad \qquad \bar{y} \le \bar{y}_{\text{u}}$$
 (5)

Where

$$a = 1 - 2n_R$$

$$b = 2n_R \frac{\bar{y}}{\bar{y}_u} - (1 - n_R) \left(1 + \frac{\bar{y}k_R}{\tilde{p}_{u,EE}} \right)$$
$$c = \frac{\bar{y}k_R}{\tilde{p}_{u,EE}} (1 - n_R) - n_p \frac{\bar{y}^2}{\bar{y}_u^2}$$

Figure 11 illustrates the shape of the conic function and its four primary variables $(k_{\rm R},\,\tilde{p}_{u,EE},\,n_{\rm R},\,\bar{y}_u)$ that depend on sand relative density and surcharge pressure as discussed later. Each of these variables in the conic function has straight-forward interpretation. For instance, the variable $k_{\rm R}$ controls the initial slope, while $\bar{y}_{\rm u}$ is the normalised displacement at which the normalised ultimate soil reaction $\tilde{p}_{u,EE}$ is attained. Beyond $\bar{y}_{\rm u}$, the $\tilde{p}_{u,EE}$ remains constant. The $n_{\rm R}$ $(0 \le n_{\rm R} \le 1)$ influences the shape of the curve; for $n_{\rm R}=0$ or 1.0, the function reduces to the bilinear forms, as seen in Figure 11.

Table 2 Calibration space encompassed by 12 combinations of surcharge pressure (σ'_v) and relative density (D_R)

D_R	$\sigma'_{\rm v}$ [kPa]	D_R	σ'_{v} [kPa]	D_R	σ' _v [kPa]
83% 50	10	65%	10	43%	10
	50		50		50
	100		100		100
	200		200		200

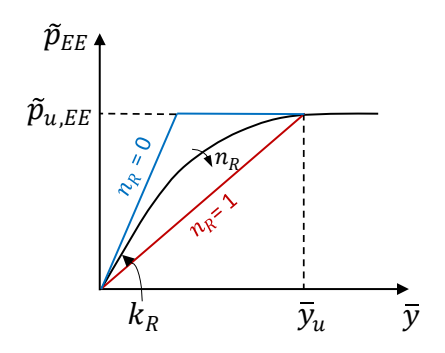


Figure 11 Illustrative diagram of the conic curve and primary governing parameters used to define the end effect of ROBOCONE p-y module

The end effect model operates by correlating the four variables in Equations (5) and (6) with the surcharge pressure and relative density, both of which can be estimated from processing of the regular CPT results. The calibration of the model followed a two-stage optimisation process, as outlined in the

337 monopiles (Burd et al. 2020). 338 **Stage 1 - Step 1:** In the first-stage optimisation, the set of variables $(k_R, \tilde{p}_{u,EE}, n_R, \bar{y}_u)$ was calculated 339 independently for each individual \tilde{p}_{EE} – y curve (from *Table 2*) by minimising the least-square error $(R_{\tilde{p}_{FF}\nu}^2)$ between the numerical data and the conic function. This process was achieved using 340 optimisation function namely fmincon() in MATLAB (Mathworks Inc. 2022). Prior to optimisation, 341 the initial value of k_R was approximated as the secant stiffness at $\bar{y} = 1\%$, while the $\tilde{p}_{u,EE}$ was 342 initially assumed to be the final increment of the numerical \tilde{p}_{EE} -y curves. In addition, the curvature 343 344 variables n_R was subjected to an upper limit of 1.0. An arbitrary \bar{y}_u values of 1.0 was adopted 345 initially and adjusted during optimisation. **Stage 1 - Step 2:** For each calibration relative density case, the dependency of the variables $(k_R, \tilde{p}_{u,EE},$ 346 n_R , \bar{y}_u) determined from Step 1 on the surcharge pressure (σ'_v) was separately identified and 347 348 predicted by the 'surcharge pressure variation function', with new variables (ζ_k, ζ_p) being 349 introduced. 350 **Stage 1 - Step 3:** The dependency of new variables (ζ_k, ζ_p) on relative density (D_R) was identified and predicted by the 'relative density variation function', with new parameters (K_{RC}, N_{RC}) being defined. 351 352 **Stage 2 - Step 4:** the aim of the second-stage optimisation is to find the optimised values of $(K_{RC}, N_{RC},$ n_R , \bar{y}_u) that perform well across the entire database to predict the p_{net} -y curves. The parameters in 353 354 the surcharge pressure and relative density variation functions were optimised, and the parameter

flow chart given in Figure 12, similar to previous work regarding the development of p-y models for

336

355

356

magnitudes from the first-stage calibration were used as initial values.

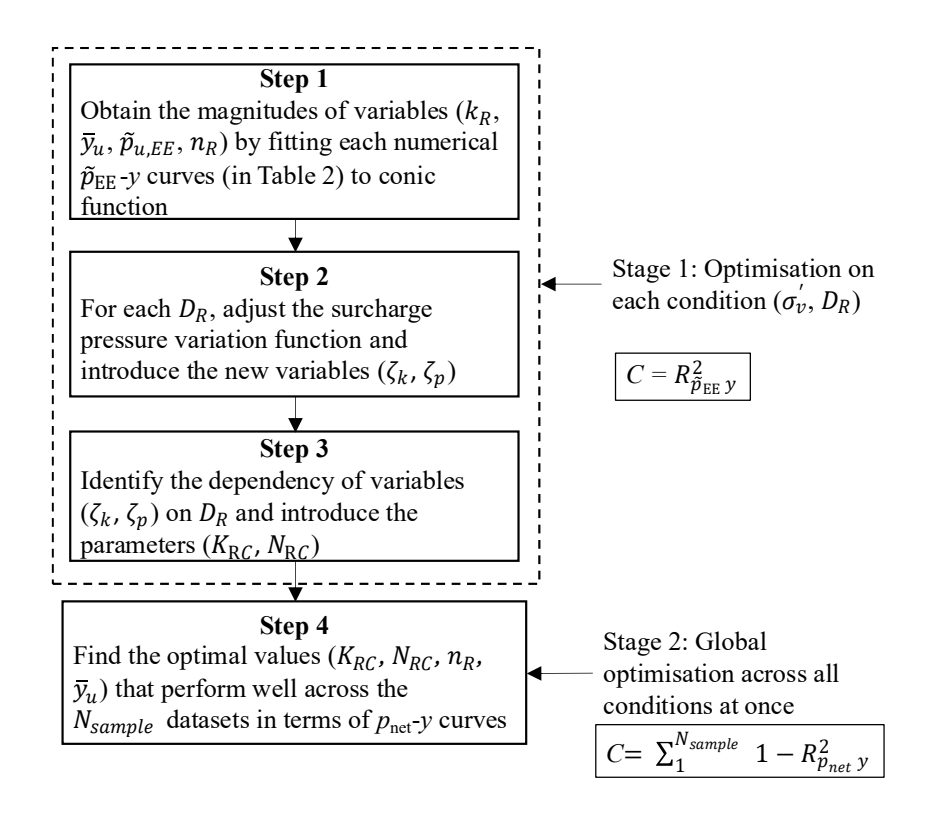


Figure 12 Two-stage optimisation process for calibration of end effect model

360 Calibration of the model: Stage 1

Figure 13 shows an example of the individual fitting of the \tilde{p}_{EE} -y curves for $D_R = 83\%$, achieving close agreement with an R^2 of 0.99. While not shown here, the other simulations for the cases in Table 2 also demonstrate excellent matches to numerical data.

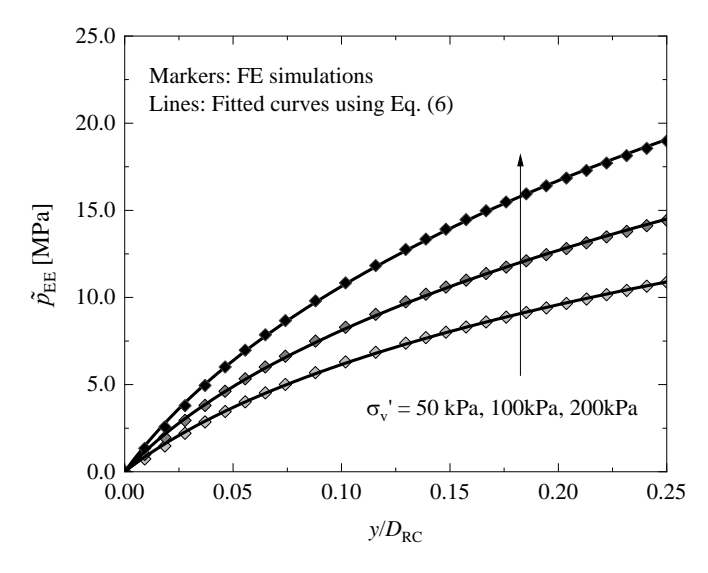


Figure 13 Individual fitting performance of the conic function ($D_R = 83\%$)

The set of primary model parameters determined for all twelve calibration cases are shown as a function of the surcharge pressures (σ'_v), which varies with the depths of p-y module test. Most calibrated \bar{y}_u parameters are close to 3 (Figure 14a), irrespective of surcharge stress and density, except two cases under $\sigma'_v = 10$ kPa, 50 kPa where \bar{y}_u values are smaller. This value represents the displacement at which the p_{EE} value becomes constant, but could not be verified explicitly, as the simulations only extend to $y/D_R = 0.35$, and the prototype p-y module has a translation limit of 20%~25% D_R (Creasey et al. 2022).

The initial stiffness k_R increases with both surcharge pressure and sand density (Figure 14(b)), as would be expected from the SANISAND-MS model where the shear modulus changes with the confining stress (p') to the power of 0.5 (see Equation (1)). To be consistent, it was assumed that the stiffness parameter k_R would increase according to the same trend,

$$k_R = \zeta_k p_{atm} \left(\frac{\sigma_v'}{p_{atm}} \right)^{0.5} \tag{7}$$

where p_{atm} is atmosphere pressure. ζ_k is a variable dependent on relative density (D_R) , to be optimised according to Step 3.

The curvature parameters n_R for both loose sand ($D_R = 43\%$) and medium dense sand ($D_R = 65\%$) fall within the range of 0.8-0.9, indicating slight variation with σ'_v (see Figure 14c). Conversely, the n_R values of dense sand show an apparent growth with the surcharge pressure. However, the n_R values seem to converge as the surcharge pressure increases irrespective of the density. For simplicity, in view of the limited value range and convergence observed, it was considered that this value could be kept constant in Step 3.

The derived ultimate end resistances at corresponding \bar{y}_u also increase with the surcharge pressure and relative density (Figure 14(d)). A fitting equation similar to the stiffness parameter was adopted:

$$\tilde{p}_{u,EE} = \zeta_p p_{atm} \left(\frac{\sigma_v'}{p_{atm}} \right)^{0.5} \tag{8}$$

Where ζ_p is a parameter associated with relative density, which will be optimised in Step 3.



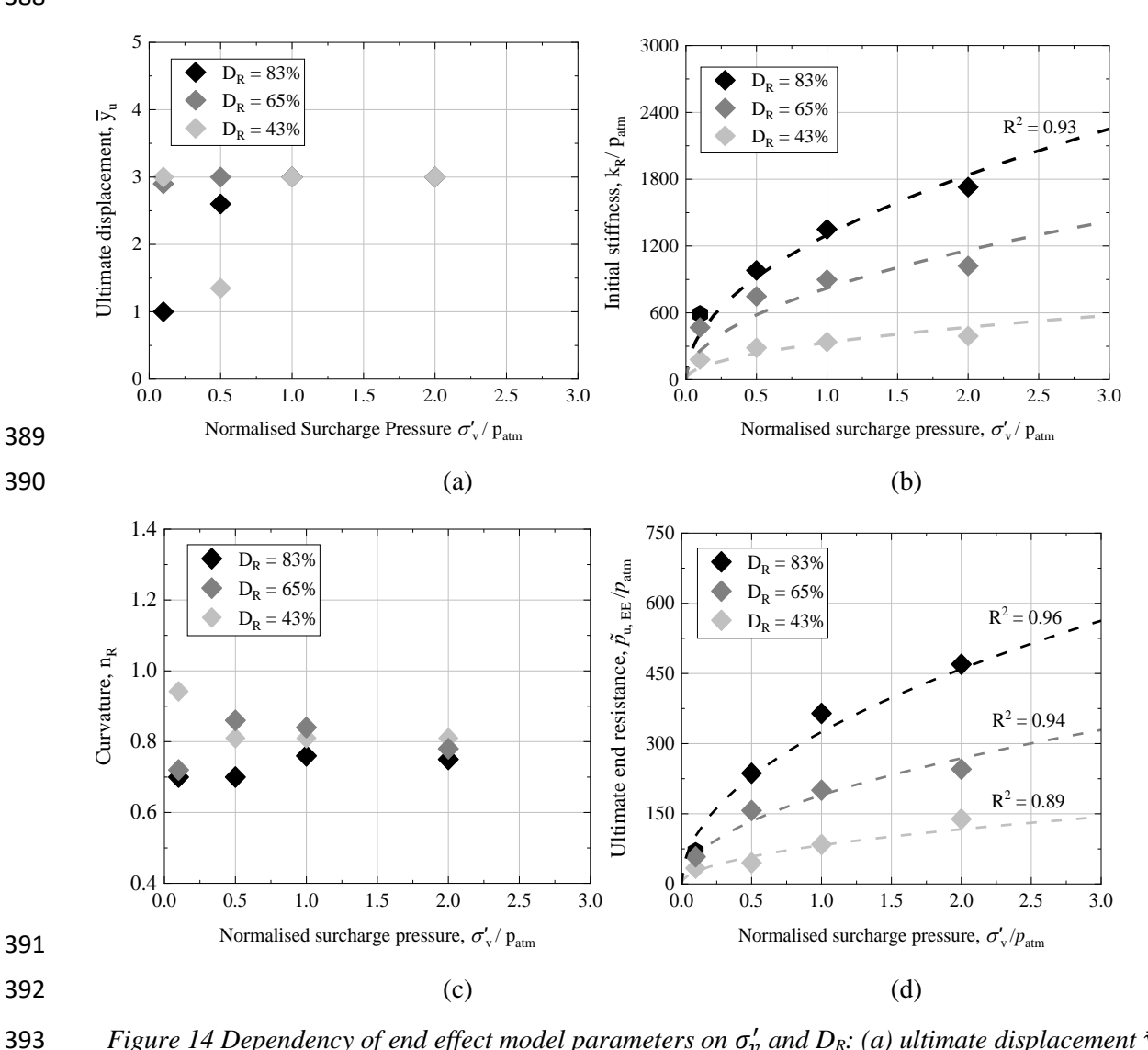


Figure 14 Dependency of end effect model parameters on σ'_v and D_R : (a) ultimate displacement \bar{y}_u ; (a) initial stiffness k_R ; (b) curvature n_R ; (c) ultimate resistance $\tilde{p}_{u,EE}$

Equations (7) and (8) introduce the new variables (ζ_k , ζ_p), which are correlated to the relative density of the sand as shown in Figure 15 and Figure 16. A simple relative density variation function was established as:

$$\zeta_k = K_{RC} D_R^2 \tag{9}$$

$$\zeta_p = N_{RC} D_R^2 \tag{10}$$

where K_{RC} is the non-dimensionless stiffness factor (= 1.82E3 in this case) and N_{RC} is the so-called bearing factor (= 470), both of which are determined from least-square fitting. The values of D_R are expressed as a decimal rather than a percentage.

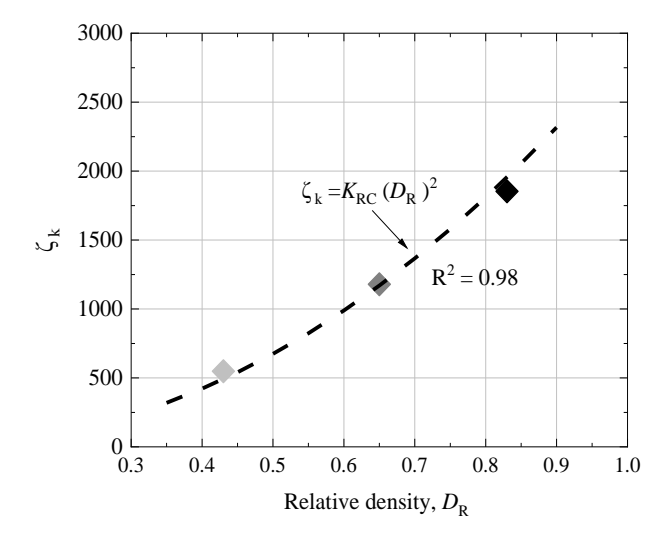


Figure 15 Power law relationship between ζ_k and relative density D_R

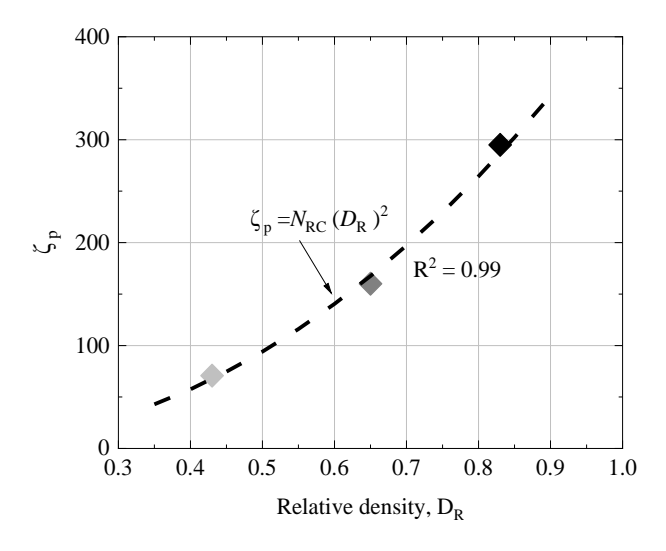


Figure 16 Relationship between ζ_p and relative density D_R

Calibration of the model: Stage 2

Equations (5)-(10) constitute the initial end effect model after the first-stage optimisation. They assume that two variables can be considered constant (\bar{y}_u and n_R) and introduce two parameters (K_{RC} and N_{RC}) in simplified equations. In the second-stage optimisation, these parameters were updated by minimising the following cost function (C),

$$C = \sum_{1}^{N_{sample}} 1 - R_{(p_{net}y)}^2 \tag{11}$$

where $N_{sample} = 12$ represents the number of datasets in the calibration space. For this second stage optimisation, it was chosen to minimise the error between the numerical p_{net} -y curves and the predicted p_{net} -y curves obtained once the ROBOCONE curves are corrected by the end effect model. This choice was made because the p_{net} -y curves represent the desired outcome of the ROBOCONE interpretation, so these provide the best measure of accuracy.

The initial values of the optimised parameters (\bar{y}_u , n_R , K_{RC} , N_{RC}) were obtained from the first-stage optimisation and all parameters were allowed to vary by up to $\pm 50\%$ of their initial values, subject to an upper limit of 1.0 on the curvature parameter n_R . This global optimisation led to an updated final set of parameters ($K_{RC} = 2.36E3$, $\bar{y}_u = 3.0$, $n_R = 0.74$, $N_{RC} = 433$).

Performance assessment of the end effect model

First, the prediction performance of the developed end effect model is assessed over the range of calibration conditions (see Table 2). The \tilde{p}_{EE} -y curves were predicted using Equations (5)-(10), whereas the p_{net} -y curves were calculated by subtracting the end effects from the direct measurement of p-y module. These two curves were compared to the numerical p_{net} -y response and the \tilde{p}_{EE} -y response. Table 3 summarises the performance metric R^2 for all calibration conditions. The average R^2 values of 0.8 and 0.9 respectively indicate a good fit of the developed end effect model to the data, with the higher relative density cases tending to produce slightly higher R^2 than the lower relative density cases.

Table 3 Summary of performance metrics of end effect model

Relative density, D_R (initial void ratio, e_0)	Surcharge pressure σ'_v [kPa]	\mathbb{R}^2	\mathbb{R}^2
	Ferrance of feet m	$(\tilde{p}_{EE}$ -y curves)	$(p_{net}$ -y curves)
	10	0.98	0.958
83% (0.60)	50	0.97	0.972
	100	0.994	0.996
	20	0.965	0.982
65% (0.67)	10	0.764	0.591

	50	0.971	0.983	
	100	0.839	0.924	
	200	0.591	0.844	
	10	0.963	0.966	
43% (0.75)	50	0.853	0.936	
	100	0.731	0.906	
	200	0.692	0.896	
Average R ²	-	0.86	0.91	

To further validate the predictive capability of the end effect model, two additional FE cases were performed at a relative density of 55%, with surcharge pressures of $\sigma'_{\rm v}=75$ kPa and 150 kPa, respectively. These conditions fall within the original calibration space but differ from the conditions employed for the calibration. Figure 17 shows the $p_{\rm net}$ -y curves and $\tilde{p}_{\rm EE}$ -y curves from numerical FE analysis, together with predictions using the developed end effect model. Values of R^2 for two cases indicate a close match between the numerical data and the predictions in terms of both the $\tilde{p}_{\rm EE}$ -y curves and the $p_{\rm net}$ -y curves. This confirms the applicability and robustness of the model developed in this study.

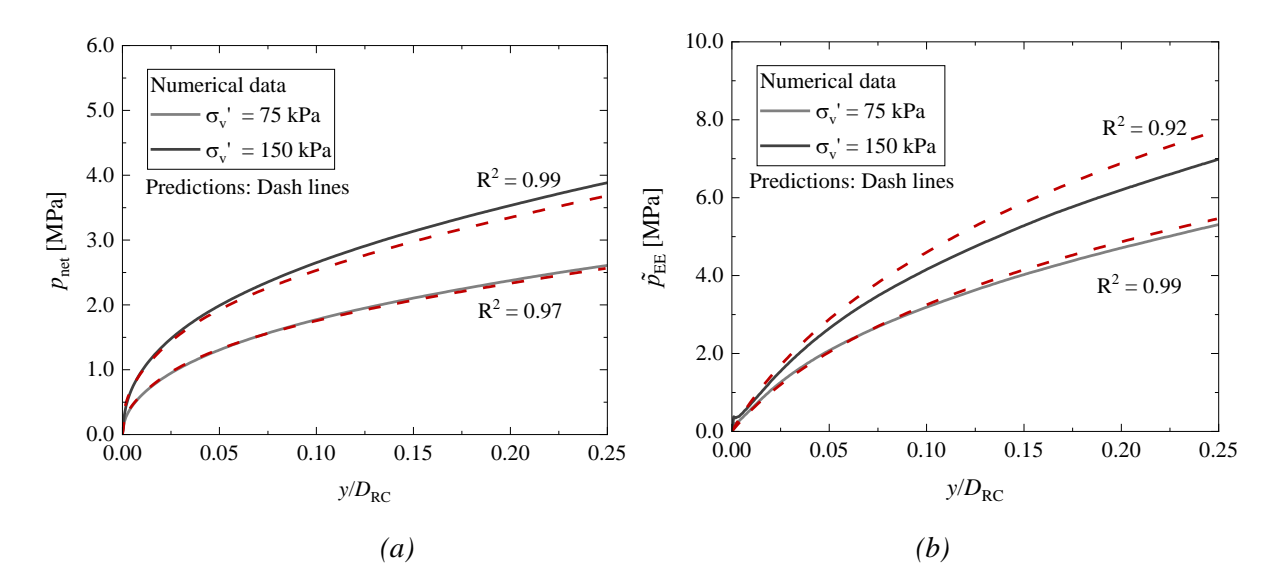


Figure 17 Performance of end effect model for additional validation cases: (a) p_{net} -y curves; (b) \tilde{p}_{EE} -y curves

APPLICABILITY OF THE END EFFECT MODEL

The main contribution of this work is to establish a generalised framework to quantify and correct the ROBOCONE data for end effects and determine p-y curves directly for foundation design. This

framework is applicable to a wider range of sand types and states, even if the model has been calibrated here using Dunkirk sand constitutive model parameters and a specific prototype ROBOCONE module $(H_{\rm RC}/D_{\rm RC}=3.7)$. In the future, the end effect model parameters can be refined as data from the field and additional simulations become available, to build confidence and reduce uncertainty in the correction factors for the ROBOCONE module, so that no further numerical simulations are necessary to interpret the data. In this way, the end effect model as presented here has similar status to equivalent correction factors and empirical correlations for other field-testing methods that often used without soil type-specific calibration (Yu 2006; Suryasentana and Lehane 2014).

However, if required, it would be possible to derive end effect model parameters tailored to a significantly different soil type – such as highly compressible carbonate sands – by rerunning a similar set of FE analyses encompassing the expected density range and stress levels. Once the end effect model is established, it enables corrections to ROBOCONE's in-situ measurement of total resistances against displacement, facilitating the generation of net resistance-displacement curves without any end effects. Considering the failure mechanism around ROBOCONE is similarly to the one that can be observed around laterally loaded piles (Wen et al. 2025), these net resistance-displacement curves can be further scaled up to determine the p-y curves for offshore pile design. However, this is beyond the scope of this study.

SUMMARY & CONCLUDING REMARKS

This study presents an interpretative framework for a new CPT module designed to probe the soil in a manner analogous to the soil surrounding laterally loaded piles. The framework eliminates the end effect of this device caused by its finite length, and reliably convert the in-situ measured response into p-y curves. The 3D finite element approach is used to simulate the behaviour of p-y module in drained sands, with the soil characterised by a bounding surface plasticity model capable of capturing the dependence of sand behaviour on relative density and stress levels. In order to visualise the end effect of the p-y module, two types of FE analyses were undertaken. In Case A, the lateral displacement is solely prescribed on the p-y module, whereas in Case B the same displacement is applied at both p-y

module and CPT shaft. Therefore, the ROBOCONE additive resistances due to end effect are determined by deducting the net ROBOCONE resistances (Case B) from the total ROBOCONE resistances (Case A). The following conclusions are reached:

- (a) The end effect becomes less important with increasing aspect ratio of the p-y module as the shaft resistance increasingly dominates the overall response.
- (b) The ratio of end resistance to total resistance is larger under lower surcharge pressure, so a higher correction is required; this ratio also varies with the relative density of the sand.
- (c) The end effect model is developed through a two-stage optimisation on the basis of fourparameter conic function, which captures the effects of relative density and surcharge pressure.
- (d) The developed end effect model can not only reproduce well the behaviour of the ROBOCONE p-y module under calibrated conditions, as indicated by the calculated error measures, but demonstrates general applicability for other validation cases that fall within the calibration space but have different from the initial conditions.
- (e) While the end effect model in this study is based on a specific aspect ratio, the framework proposed in this study to optimise the model parameters can be applied to a p-y module with other aspect ratios.

In summary, this study provides the interpretation framework required to convert the results from the p-y module to the p-y curves for pile design. This supports greater use of such in-situ test data for offshore design, without recourse to subsequent onshore laboratory testing, and therefore contributes towards shorter timeframes for offshore project developments. Future work will extend the current monotonic end effect model by incorporating complex cyclic loading conditions. This will leverage the advantages of memory surface components within the SANISAND-MS model.

ACKNOWLEDGEMENT

The authors would like to acknowledge the financial support from the Engineering and Physical Sciences Research Council (Ref: EP/W006235/1: ROBOCONE – intelligent robotics for next generation ground investigation and design) and Science Foundation Ireland (SFI - Ref: 21/EPSRC/3787). Susan Gourvenec is supported through the Royal Academy of Engineering Chair in Emerging Technologies Scheme. David White is also supported through the EPSRC Offshore Renewable Energy Supergen Hub (EPSRC – Ref: EP/Y016297/1).

REFERENCES

API (2014). Recommended Practice 2GEO-Geotechnical and Foundation Design Considerations, American Petroleum Institute. Washington, DC, USA: American Petroleum Institute.

Burd, H. J., Taborda, D. M., Zdravković, L., Abadie, C. N., Byrne, B. W., Houlsby, G. T., ... & Potts, D. M. (2020). PISA design model for monopiles for offshore wind turbines: application to a marine sand. Géotechnique, 70(11), 1048-1066.

Climate Change Committee (2020). The Sixth Carbon Budget: the UK's path to Net Zero (London, UK).

Creasey, J. et al. (2023). Motivation and demonstration of robotic tolling for ground characterisation: the ROBOCONE. Proceedings of the 9th Int. Conf. on Offshore Site Investigations and Geotechnics, pp. 368-375. London, UK: Soc. Underwater Tech.

Dafalias, Y. F. & Manzari, M. T. (2004). Simple plasticity sand model accounting for fabric change effects. Journal of Engineering Mechanism. 130, No. 6, 622–634.

DeJong, J.T. and Frost, J.D. (2002). A multi-friction sleeve attachment for the cone penetrometer. ASTM Geotechnical Testing Journal, 25(2):111–127.

Diambra, A., Creasey, J., Leonet, J., Conn, A., Ibraim, E., Mylonakis, G., White, D., Cerfontaine, B., Gourvenec, S., & Igoe, D. (2022). Concept design of a new CPT module for direct in situ measurement of py soil responses. In *Cone Penetration Testing* 2022 (pp. 900-906). CRC Press.

DNV GL (2016). DNVGL-ST-0126 – Support structure for wind turbines. Oslo, Norway: DNV GL.

Frost, J. D., & Martinez, A. (2013). Multi-sleeve axial-torsional-piezo friction penetration system for subsurface characterization. In Proceedings of the 18th International Conference on Soil Mechanics and Geotechnical Engineering (Vol. 1, pp. 527-530).

Greaves, D.; White, D.; Noble, D.; Jeffrey, H.; Gilbert, J.; Zhao, X.; Byrne, B.; Willden, R.; Stallard, T.; Mullings, H.; Scott, B.; Brennan, F.; Thies, P.; Richards, L.; Henderson, K.; Mascall, R. (2024). ORE Outlook 2040 - UK Offshore Renewable Energy in 2040: Building a Sustainable and Competitive ORE Sector on a Pathway to Net Zero by 2050. Report by Supergen Offshore Renewable Energy Hub.

Guo, F., & Lehane, B. M. (2016). Lateral response of piles in weak calcareous sandstone. Canadian Geotechnical Journal, 53(9), 1424-1434.

Jeanjean, P (2009). Re-assessment of P–Y curves for soft clays from centrifuge testing and finite element modeling. In: Offshore technology conference.

Jostad, H. P., Dahl, B. M., Page, A., Sivasithamparam, N., & Sturm, H. (2020). Evaluation of soil models for improved design of offshore wind turbine foundations in dense sand. Géotechnique, 70(8), 682-699.

Lehane, B.M. (2019). CPT-based design of foundations. E.H. Davis Memorial Lecture (2017), Australian Geomechanics, 54(4), 23-48

Liu, H. Y., Abell, J. A., Diambra, A. & Pisanò, F. (2019). Modelling the cyclic ratcheting of sands through memory-enhanced bounding surface plasticity. *Géotechnique* 69, No. 9, 783–800.

Loukidis, D. & Salgado, R. (2009). Modeling sand response using two-surface plasticity. *Comput. Geotech.* 36, No. 1–2, 166–186.

Mahmoodzadeh, H., Wang, D., & Randolph, M. F. (2015). Interpretation of piezoball dissipation testing in clay. Géotechnique, 65(10), 831-842.

MathWorks Inc. (2022). Statistics and Machine Learning Toolbox Documentation, Natick, Massachusetts: The MathWorks Inc.

Matlock, H. (1970). Correlations for design of laterally loaded piles in soft clay. Proceedings of the 2nd annual offshore technology conference, Houston, TX, USA, vol. 1, paper no. OTC 1204, pp. 577–594.

Pisanò, F., Del Brocco, I., Ho, H. M., & Brasile, S. (2024). 3D FE simulation of PISA monopile field tests at Dunkirk using SANISAND-MS. Géotechnique Letters, 1-30.

Randolph, M. F. & Andersen, K. H. (2006). Numerical simulation of T-bar penetration in soft clay. Numerical analysis of T-bar penetration in soft clay. International Journal of Geomechanics 6.6: 411-420.

Reese, L.C., Cox, W.R., Koop, F.D. (1974). Analysis of laterally loaded piles in sand. In: Proc., 6th Offshore Technology Conf., Houston, OTC-2080-MS, 473-483.

Stanier, S. A., & White, D. J. (2019). Enhancement of bearing capacity from consolidation: due to changing strength or failure mechanism? *Géotechnique*, 69(2), 166-173.

Suryasentana S. and Lehane B.M. (2014). Numerical derivation of CPT-based p-y curves for piles in sand. *Géotechnique*, 64(3), 186-194.

Taborda, D. M., Zdravković, L., Potts, D. M., Burd, H. J., Byrne, B. W., Gavin, K. G., ... & McAdam, R. A. (2020). Finite-element modelling of laterally loaded piles in a dense marine sand at Dunkirk. *Géotechnique*, 70(11), 1014-1029.

Truong, P., & Lehane, B. (2014). Numerically derived CPT-based py curves for a soft clay modeled as an elastic perfectly plastic material. In 3rd International Symposium on Cone Penetration Testing (pp. 975-982). International Symposium on Cone Penetration Testing.

Wang, Y., Hu, Y., Hossain, M. S., & Zhou, M. (2020). Effect of trapped cavity mechanism on interpretation of T-Bar penetrometer data in uniform clay. Journal of Geotechnical and Geoenvironmental Engineering, 146(9), 04020078.

Wen, K., Cerfontaine, B., White, D., Gourvenec, S., & Diambra, A. (2024). Lateral bearing factors and elastic stiffness factors for robotic CPT py module in undrained clay. *Computers and Geotechnics*, 172, 106487.

White, D. J. (2022). CPT equipment: Recent advances and future perspectives. In *Cone Penetration Testing* 2022, (pp. 66-80). CRC press

Yan, Y., White, D. J., & Randolph, M. F. (2011). Penetration resistance and stiffness factors for hemispherical and toroidal penetrometers in uniform clay. *Int. J. Geomechanics*, 11(4), 263-275.

Yu, H. S. (2006). The First James K. Mitchell Lecture In situ soil testing: from mechanics to interpretation. *Geomechanics and Geoengineering*, 1(3), 165-195.

Zdravkovic´, L., Jardine, R. J., Taborda, D. M. G., Burd, H. J., Byrne, B. W., Gavin, K. G., Houlsby, G. T., Igoe, D. J. P., Liu, T., Martin, C. M., McAdam, R. A., Muir Wood, A., Potts, D. M., Skov Gretlund, J. & Ushev, E. (2020). Ground characterisation for PISA pile testing and analysis. *Géotechnique*. 70(11), 945-960.

Zhou, M., Hossain, M. S., Hu, Y., & Liu, H. (2013). Behaviour of ball penetrometer in uniform single-and double-layer clays. Géotechnique, 63(8), 682-694.

LIST OF FIGURES

Figure 1 Schematic illustration of ROBOCONE p-y module (adapted from Diambra et al. 2022)

Figure 2 Finite element model of the p-y module prototype (H_{RC} / D_{RC} = 3.7) embedded in soil assembly with mesh, loading and boundary conditions

Figure 3 Schematic illustration of SANISAND-MS model surfaces (a) in p '-q space; (b) in the deviatoric stress ratio plane (modified after PLAXIS (2023))

Figure 4 Performance of SANISAND-MS model on predicting the drained triaxial compression behaviour of Dunkirk sand (adapted from Pisanò et al. 2024)

Figure 5 Determination of end effects from comparison of FE analysis cases

Figure 6 Monotonic loading response of p-y module with various aspect ratios ($\sigma v' = 200 \text{ kPa}$; $D_R = 200 \text{ kPa}$).

83%): (a) p_{tot} -y curves; (b) p_{net} -y curves; (c) p_{EE} -y curves

Figure 7 Variation of end resistance with increasing lateral displacement and ROBOCONE p-y module aspect ratios ($\sigma v' = 200 \text{ kPa}$)

Figure 8 Impact of surcharge pressure $\sigma v'$ on the p-y module response (H_{RC}/D_{RC} = 3.7; D_R = 83%): (a) total resistances p_{tot}; (b) net resistances p_{net}; (c) end effect resistances p_{EE}

Figure 9 Fields of cumulative vertical soil displacement at $y/D_{RC} = 20\%$: (a) $H_{RC}/D_{RC} = 3.7$; (b)

 $H_{RC}/D_{RC} = 8.0$; (c) $H_{RC}/D_{RC} = 16.0$

Figure 10 Fields of current void ratio at $y/D_{RC} = 20\%$: (a) $H_{RC}/D_{RC} = 3.7$; (b) $H_{RC}/D_{RC} = 8.0$; (c) $H_{RC}/D_{RC} = 16.0$

Figure 11 Illustrative diagram of the conic curve and primary governing parameters used to define the end effect of ROBOCONE p-y module

Figure 12 Two-stage optimisation process for calibration of end effect model

Figure 13 Individual fitting performance of the conic function ($D_R = 83\%$)

Figure 14 Dependency of end effect model parameters on $\sigma v'$ and D_R : (a) ultimate displacement yu;

(a)initial stiffness kR; (b) curvature nR; (c) ultimate resistance pu, EE

Figure 15 Power law relationship between ζk and relative density DR

Figure 16 Relationship between ζp and relative density DR

Figure 17 Performance of end effect model for additional validation cases: (a) p_{net} -y curves; (b) pEE-y curves

LIST OF TABLES

Table 1 SANISAND-MS model parameters calibrated for Dunkirk sands (Pisanò et al. 2024) as used in this study

Table 2 Calibration space encompassed by 12 combinations of surcharge pressure (σv ') and relative density (DR)

Table 3 Summary of performance metrics of end effect model